

Article

Ascending Performance of Scientific Balloons with Buoyant Gas–Air Mixture Inflation for Designated Ceiling Height

Shenghong Cao^{1,2,*} , Yanchu Yang^{1,2,*}, Hangyue Zhang¹, Rong Zhao¹, Rongchen Zhu¹, Donghui Zhang¹ and Lin Song¹

¹ Aerospace Information Research Institute, Chinese Academy of Sciences, Beijing 100094, China

² University of Chinese Academy of Sciences, Beijing 100190, China

* Correspondence: caoshenghong20@mails.ucas.ac.cn (S.C.); yangyanchu@aoe.ac.cn (Y.Y.)

Abstract: This paper aims to investigate a new method that uses buoyant gas mixed with air to control the floating height of scientific balloons. Firstly, the static characteristics and thermophysical properties of mixed-gas balloons are analyzed. Subsequently, the inflation model and the thermal-dynamic coupled model are established. Furthermore, based on theoretical research, a GUI program is compiled to simulate the ascent of mixed-gas balloons. Finally, flight tests are conducted. As the balloon volume expands to the maximum, the vertical velocity begins to decay and eventually oscillates around 0 m/s, which is consistent with the simulation. In addition, there is a noticeable shift in which the balloon starts to float after climbing to the target altitude, and the difference values between the test and the simulation are less than 350 m. Moreover, the trajectory results are similar to the prediction, and the errors of the end position are less than 2.5 km in horizontal distance. Consequently, this paper provides guidance for balloon-designated ceiling height technology which can allow a single balloon system to be used for tests at multiple heights.

Keywords: scientific balloons; designated ceiling height; air–buoyant gas mixture; trajectory prediction



Citation: Cao, S.; Yang, Y.; Zhang, H.; Zhao, R.; Zhu, R.; Zhang, D.; Song, L. Ascending Performance of Scientific Balloons with Buoyant Gas–Air Mixture Inflation for Designated Ceiling Height. *Aerospace* **2024**, *11*, 340. <https://doi.org/10.3390/aerospace11050340>

Academic Editors: Alberto Rolando and Carlo E. D. Riboldi

Received: 28 March 2024

Revised: 22 April 2024

Accepted: 22 April 2024

Published: 25 April 2024



Copyright: © 2024 by the authors. Licensee MDPI, Basel, Switzerland. This article is an open access article distributed under the terms and conditions of the Creative Commons Attribution (CC BY) license (<https://creativecommons.org/licenses/by/4.0/>).

1. Introduction

Aerostat is a lighter-than-air vehicle [1] that carries payloads to perform various scientific missions in high-altitude environments. Many institutions have conducted research on several key technologies such as design, materials, stability, and autonomous operation [2,3]. Meanwhile, some scholars have utilized virtual simulations to validate conceptual designs and aid engineers in addressing challenges [4]. The scientific balloon is one type of aerostat. Compared to other aircraft, the balloon exhibits exceptional stability in high-altitude environments [5]. Hence, balloons are widely used for the collection and analysis of atmospheric parameters [6,7]. For instance, the National Climatic Data Center (NCDC) has established the Integrated Radio Sounding Archive (ICAR), which is valuable in the fields of weather forecasting, stratospheric temperature and humidity trend assessment, and validation of measurements from other platforms [8,9]. In addition, high-altitude balloons are widely used in scientific observation and regional communication [10–14]. Moreover, high-altitude balloons can serve as a platform for launching UAVs [15,16] and carry payloads to explore other planets [17–20].

According to the pressure difference value between the inside and outside, balloons can be classified into super-pressure balloons (SPBs) and zero-pressure balloons (ZPBs) [21–23]. The ZPB structure incorporates exhaust pipes that connect with the environment to maintain the equal internal–external pressures. Conversely, the SPB is closed, and the film bears the pressure. The mixed-gas balloon in this paper is an SPB because the structure is essentially closed during flight.

SPBs can float for a long period, which is an important requirement for stratospheric exploration by the National Aeronautics and Space Administration (NASA) [24]. Consequently, NASA conducts research on many topics—including studying the phenomenon

of incomplete unfolding and the stability of the SPB—which are invaluable for balloon design and materials selection [25]. Additionally, the French National Centre for Space Studies (CNES) has more than 20 years of research experience in balloon engineering, including the CONCORDIASI project, which conducted 19 flights over Antarctica from September 2010 to January 2011. CONCORDIASI built an accurate thermal model that studied the effects of solar irradiation on different balloon materials [26]. On this basis, CNES conducted the STRATEOLE-2 project, which launched eight balloons between 11 November and 7 December 2019. These flights lasted several months and demonstrated the effectiveness of the system.

It is noteworthy that micro SPBs have demonstrated remarkable achievements in recent years. Between the winter of 2021 and the summer of 2023, students from the University of Alabama conducted several micro SPB global voyage experiments [27–29]. The experiments collected a large amount of invaluable data for atmospheric studies. These experiments also demonstrated that the micro SPBs can float at lower altitudes, which provides a unique perspective on the interaction between the troposphere and stratosphere.

Designing balloon systems for missions at varying floating heights necessitates distinct designs, leading to high costs for design and manufacturing. As depicted in Figure 1, this paper introduces innovative research that adjusts the air and lighter-than-air gas mixture proportions to regulate the floating height. This novel approach allows a single balloon system to be used for tests at multiple heights, thereby reducing the costs.

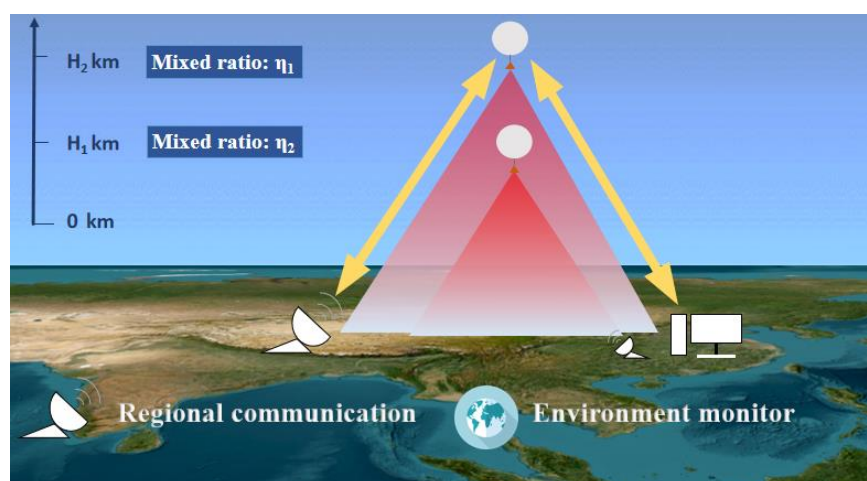


Figure 1. Schematic diagram of the application of mixed-gas balloons.

Figure 1 illustrates the application scenarios of mixed-gas balloons. A larger air ratio causes the balloon to float at a lower height. Conversely, a smaller air ratio causes the balloon to float at a higher height. Therefore, the air ratio determines the mixed-gas balloon’s ability to float at different altitudes for scientific missions.

Firstly, the inflation model is provided based on the Buoyancy Weight Balance and the Ideal Gas Equation. Furthermore, a thermal-dynamic coupled model is presented. Subsequently, a GUI program is used to simulate the ascent of the mixed-gas balloon. Finally, this paper reports on flight tests, the results of which verify that an air–buoyant gas mixture for designated ceiling height technology is feasible.

Trajectory prediction holds significant engineering importance. However, the existing literature lacks research on the ascent of mixed-gas balloons, making it urgent to predict the ascending trajectory of mixed-gas balloons in engineering. Consequently, this paper systematically analyzes the thermal-dynamic environment of mixed-gas balloons. Meanwhile, this paper establishes a feasible theoretical model, which is invaluable for the reliability and safety of mixed-gas balloons.

2. Theoretical Model

2.1. Inflation Model

Combined with the Buoyancy Weight Balance of the balloon at target height and the Ideal Gas Equation, we propose an inflation model which can calculate the inflation of the air and buoyant gas. Meanwhile, the model applies to different size balloons and different types of gas mixtures (Air–Hydrogen, Air–Helium, etc.)

The balloon is mainly affected by buoyancy and gravity at target height and reaches the balance, as shown in Equation (1).

$$\rho_{air}V = m_{gas} + m_{air} + m_{balloon} + m_{payload} \quad (1)$$

The Ideal Gas Equation is shown in Equation (2).

$$\rho = \frac{P}{R \cdot T} \quad (2)$$

According to Equations (1) and (2), the inflation model is shown in Equation (3).

$$\eta = \left[\frac{P_{target} \cdot V}{R_{air} \cdot T_{target}} - m_{balloon} - m_{payload} - m_{gas} \right] / m_{gas} \quad (3)$$

P_{target} and T_{target} are the ambient pressure and temperature at the target altitude.

2.2. Thermal Physics Properties

2.2.1. Heat Transfer Coefficient

Before studying the thermal model, this paper analyzes the thermo-physical properties of the gas mixture. The heat transfer coefficient is an important parameter of the thermal model, which will directly affect the heat-exchange process. Many scholars have studied the heat-transfer coefficient of the mixture, which has greatly improved calculation accuracy. Based on the Wilke [30] equation, Tong [31] studied the heat transfer coefficient of the mixed gas as follows.

$$k_{mix} = \sum_{i=1}^n \frac{k_i}{1 + \sum_{\substack{j=1 \\ j \neq i}}^n G_{ij} \frac{y_j}{y_i}} \quad (4)$$

y is the molecular fraction; G is the binding coefficient; and the subscripts i and j represent different gas compositions. The calculation is shown in Equation (5).

$$G = \varepsilon \cdot \phi \quad (5)$$

ε is the correction coefficient; ϕ is the Interaction coefficient.

2.2.2. Heat Capacity

The gas mixture still obeys Dalton's law and Amagat's law [32], which are shown in Equations (6) and (7).

$$P = P_1 + P_2 + P_3 + \dots + P_n = \sum_{i=1}^n P_i \quad (6)$$

$$V = V_1 + V_2 + V_3 + \dots + V_n = \sum_{i=1}^n V_i \quad (7)$$

In addition, this paper defines the components of mass and volume, which guide the calculation of the heat capacity as follows:

$$g_n = \frac{m_n}{m} \quad (8)$$

$$r_n = \frac{V_n}{V} \tag{9}$$

The mass specific heat c and volume specific heat c' are given as follows:

$$c = g_1c_1 + g_2c_2 + g_3c_3 + \dots + g_nc_n = \sum_{i=1}^n g_i c_i \tag{10}$$

$$c' = r_1c'_1 + r_2c'_2 + r_3c'_3 + \dots + r_nc'_n = \sum_{i=1}^n r_i c'_i \tag{11}$$

2.2.3. Balloon Model

The volume calculation is shown in Equation (12).

$$\begin{cases} V_{balloon} = V_{gas} + V_{air} \\ \frac{V_{gas}}{V_{air}} = \frac{m_{gas}}{m_{air}} \cdot \frac{R_{gas}}{R_{air}} \end{cases} \tag{12}$$

Before the balloon volume reaches its maximum, the pressure inside and outside the balloon are equal. As the balloon volume expands to the maximum, the pressure inside the balloon can be greater than that outside of the balloon at this point.

The balloon shape is assumed to be spherical and the effective surface area and the top projection area [33,34] are shown in Equation (13).

$$\begin{cases} A_{eff} = \pi Diameter^2 \\ A_{top-project} = \frac{1}{4} \pi Diameter^2 \end{cases} \tag{13}$$

Dimeter is the balloon dimeter as follows:

$$Diameter = 1.23V_{balloon}^{\frac{1}{3}} \tag{14}$$

2.2.4. Thermal Environment

The thermal environment will affect the force on the balloon, and it has been an area of focus for scholars. Based on references [33,35–39], this paper further analyzes the thermal environment of the mixed-gas balloon. As shown in Figure 2, the balloon is mainly affected by solar radiation, ground radiation, sky radiation, and convective heat transfer during ascent.

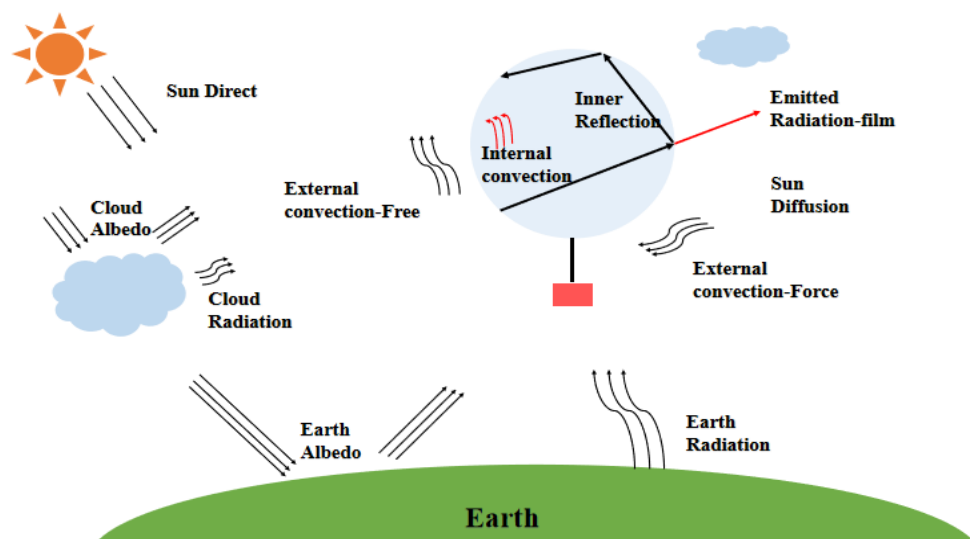


Figure 2. Thermal environment.

1. Solar radiation

(1) Solar radiation on the film [33]

The solar radiation on the film includes direct and reflected radiation, which are shown in Equations (15) and (16).

$$Q_{sun-direct} = \alpha A_{top-project} q_{sun} [1 + \tau(1 + r_{eff})] \quad (15)$$

$$Q_{sun-reflect} = \alpha A_{eff} q_{Albedo} \tau_{ViewFactor} [1 + \tau(1 + r_{eff})] \quad (16)$$

q_{sun} is the direct solar flux [34,40], which can be formulated as follows.

$$q_{sun} = \begin{cases} I_{sun,z}(1 - CF) & z \leq 11000 \text{ m} \\ I_{sun,z} & z > 11000 \text{ m} \end{cases} \quad (17)$$

CF is the cloud factor [34]; $I_{sun,z}$ is the resultant solar intensity as follows:

$$I_{sun,z} = I_{sun} \cdot \tau_{atm} \quad (18)$$

I_{sun} is the total solar intensity; τ_{atm} is the atmospheric transmittance [34].

In Equation (16), q_{Albedo} is the allowable albedo intensity [33] which is shown in Equation (19).

$$q_{Albedo} = Albedo \cdot I_{sun} \cdot \sin(\alpha_{ELV}) \quad (19)$$

$Albedo$ is the albedo factor [33]; α_{ELV} is the solar elevation angle [34,41] as follows:

$$\alpha_{ELV} = \arcsin[\sin \delta \sin \varphi + \cos \delta \cos \varphi \cos(HRA)] \quad (20)$$

δ is the declination angle; φ is the location latitude; HRA is the hour angle.

(2) Solar radiation on the balloon gas [34,42]

The solar radiation on the balloon gas includes direct and reflected solar radiation, and the formulation is shown in Equation (21) [34,42].

$$Q_{sun-gas} = \alpha_{eff-gas} \cdot A_{eff} \cdot q_{sun} \cdot (1 + Albedo) \quad (21)$$

$\alpha_{eff-gas}$ is the effective solar absorption factor of the balloon gas.

2. Infrared radiation from the Earth and sky

(1) The effective IR radiation absorbance of the balloon film

$$Q_{IR-earth\&sky} = \varepsilon_{eff} \cdot \sigma \cdot A_{eff} \cdot T_{BB}^4 \quad (22)$$

ε_{eff} is the effective emissivity factor; σ is the Stefan–Boltzmann Number.

(2) The effective IR radiation absorbance of the balloon gas [42]

$$Q_{IR-earth\&sky-gas} = \varepsilon_{eff-gas} \cdot \sigma \cdot A_{eff} \cdot T_{BB}^4 \quad (23)$$

$\varepsilon_{eff-gas}$ is the effective gas emissivity factor.

3. The thermal interchange of the film [34]

$$Q_{IR-int} = \varepsilon_{int} \cdot \sigma \cdot A_{eff} \cdot (T_{gas}^4 - T_{film}^4) \quad (24)$$

ε_{int} is the interchange effective emissivity factor.

4. Balloon film emits heat radiation

$$Q_{IR-emit} = \varepsilon_{eff} \cdot \sigma \cdot A_{eff} \cdot T_{film}^4 \quad (25)$$

5. The heat emission of the balloon gas

$$Q_{IR-emit-gas} = \varepsilon_{eff-gas} \cdot \sigma \cdot A_{eff} \cdot T_{gas}^4 \quad (26)$$

6. External convection

The external convection occurs between the air and film [34] as follows:

$$Q_{con-ext} = HC_{external} \cdot A_{eff} \cdot (T_{air} - T_{film}) \quad (27)$$

$HC_{external}$ is the effective external convection, including free convection and forced convection [42–45].

$$HC_{external} = (H_{force}^3 + H_{free}^3)^{\frac{1}{3}} \quad (28)$$

7. Internal convection [34]

The internal convection occurs between the balloon gas and film as follows:

$$Q_{con-int} = HC_{internal} \cdot A_{eff} \cdot (T_{film} - T_{gas}) \quad (29)$$

2.2.5. Thermal Differential Equation

1. Balloon gas differential equation

The temperature of balloon gas is mainly affected by solar radiation, environmental radiation, and convective heat as shown in Equation (30).

$$\frac{dT_{gas}}{dt} = \frac{1}{c_v \cdot m_{gas}} (Q_{sun-gas} - Q_{IR-int-gas} + Q_{IR-earth\&sky-gas} - Q_{con-int} - Q_{IR-emit-gas}) + (\gamma - 1) \cdot T_{gas} \left(\frac{dm_{gas}}{dt} \cdot \frac{1}{m_{gas}} - \frac{dV}{dt} \cdot \frac{1}{V} \right) \quad (30)$$

$\frac{dm_{gas}}{dt}$ is the balloon gas mass differential which depends on the exhaust valve [33].

$$\frac{dm_{gas}}{dt} = -A_{valve} \cdot C_{discharge} \cdot \sqrt{2 \cdot \Delta P_{valve} \cdot \rho_{gas}} \quad (31)$$

2. Balloon film differential equation

The temperature of the balloon film is also affected by solar radiation, environmental radiation, and convective heat as shown in Equation (32).

$$\frac{dT_{film}}{dt} = \frac{Q_{sun} + Q_{IR-int} + Q_{IR-earth\&sky} + Q_{con-ext} - Q_{int} - Q_{IR-emit}}{c_{film} \cdot m_{film}} \quad (32)$$

2.3. Dynamic Model

2.3.1. Force Analysis

Velocity, altitude, and trajectory are important reference indexes of the balloon. The mixed-gas balloon is mainly affected by buoyancy, drag force, and gravity during ascent.

The launch point is taken as the origin O, and the vertical direction of the balloon is the positive direction of the Z axis. The south direction is the positive direction of the X axis, and the east direction is the positive direction of the Y axis.

The velocity is $v(u, v, w)$; the wind velocity is v_w . The relative velocity is v_r .

$$v_r = v_w - v \quad (33)$$

The forces on the balloon during ascent are analyzed as follows.

In Figure 3, F_B is the total buoyancy as shown in Equation (34).

$$F_B = \rho_a \cdot g \cdot V \quad (34)$$

D_x, D_y, D_z are the wind drag force of three directions [33] as follows.

$$D = \frac{1}{2} \cdot \rho_{air} \cdot v_r^2 \cdot C_D \cdot S \tag{35}$$

C_D is the drag coefficient [46,47], which is related to the Reynolds number.

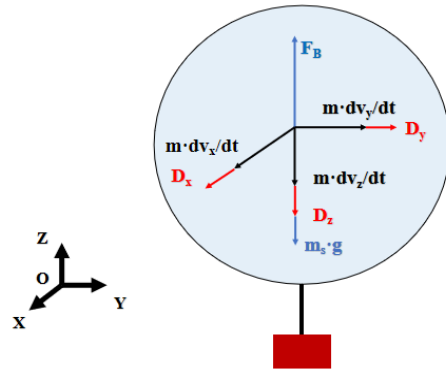


Figure 3. Force analysis during ascent.

2.3.2. Vertical Direction Difference Model

The balloon is mainly affected by buoyancy, gravity, and drag force in the vertical direction, which is shown in Equation (36).

$$\begin{cases} \frac{dw}{dt} = (F_B - D_z - m_s \cdot g) / m \\ \frac{dz}{dt} = w \end{cases} \tag{36}$$

m_s is the system mass that includes the mass of the structure and balloon gas.

$$m_s = m_{balloon-structure} + m_{balloon-gas} \tag{37}$$

In Equation (36), m is the equivalent mass of the system, which includes the total mass and the added mass. The added mass is generated by the surrounding air movement which is caused by the balloon [33].

$$m_v = C_m \cdot \rho_{air} \cdot V \tag{38}$$

C_m is the additional mass coefficient, which is related to the balloon shape [48,49].

2.3.3. X/Y Direction Difference Model

The balloon is mainly affected by surrounding wind drag in the X/Y direction, which is calculated as shown in Equation (39).

$$\begin{cases} \frac{du}{dt} = (D_x) / m \quad \frac{dv}{dt} = (D_y) / m \\ \frac{dx}{dt} = u \quad \frac{dy}{dt} = v \end{cases} \tag{39}$$

3. Simulation

3.1. Simulation Program Framework

Combined with the above theoretical models, this paper establishes a simulation program framework as follows.

As shown in Figure 4, the framework comprises input, operation model, and output. The input consists of balloon parameters, material properties, and launch parameters. The computational part includes the inflation model and thermal-dynamic coupled model. In addition, to ensure simulation accuracy, meteorological balloon-sounding data is incorporated. The output includes dynamic parameters and thermodynamic parameters.

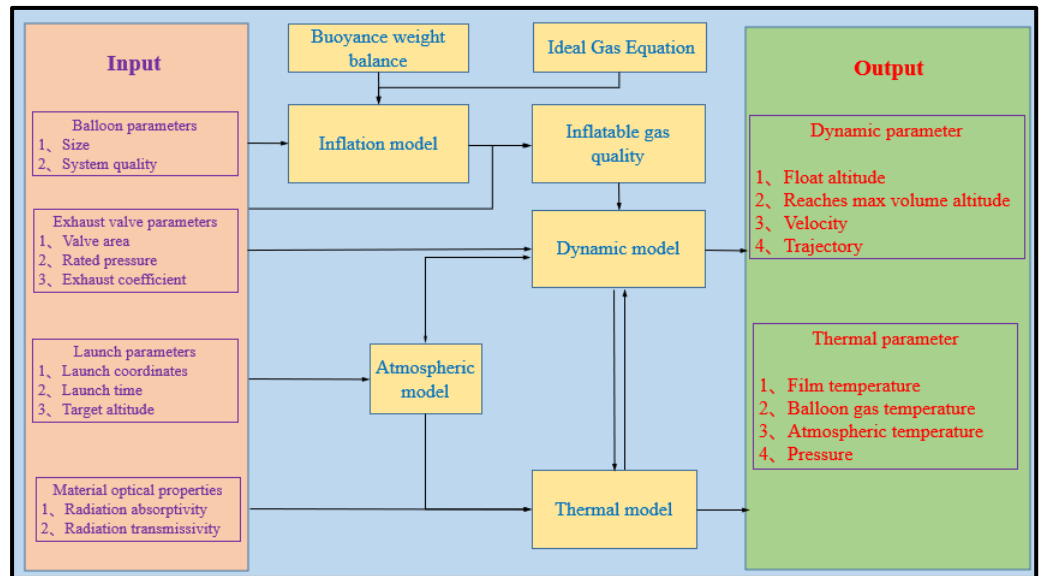


Figure 4. The simulation framework.

3.2. GUI Program

Based on the program framework, this paper uses MATLAB to simulate the ascent of the mixed-gas balloon. In addition, considering the application requirements, a GUI program is established which can observe and analyze the simulation results intuitively, as shown in Figure 5.

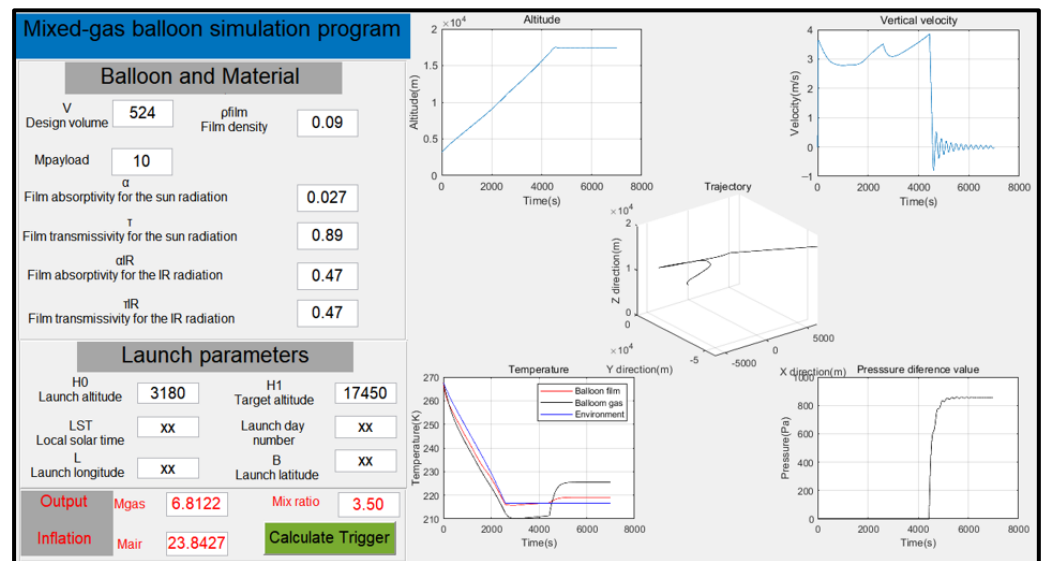


Figure 5. The GUI interface of the mixed-gas balloon.

As shown in Figure 5, the mixed-gas balloon simulation GUI program interface is divided into an input module and an output module. The left side is the input module, including the design parameters. The right side is the output module, which is convenient for comparative analysis of various conditions intuitively.

3.3. Balloon Parameters

Before the simulation, this paper gives the design parameters, which are shown in Tables 1–3.

Table 1. Balloon parameters.

Parameter	Value
Design volume (m ³)	524.0
Design diameter (m)	10.0
The mass of the film (kg)	28.28
The mass of the payload (kg)	10.00

Table 2. Optical properties of the film material.

α	τ	α_{IR}	τ_{IR}
0.027	0.890	0.470	0.470

The optical properties were obtained from the manufacturer.

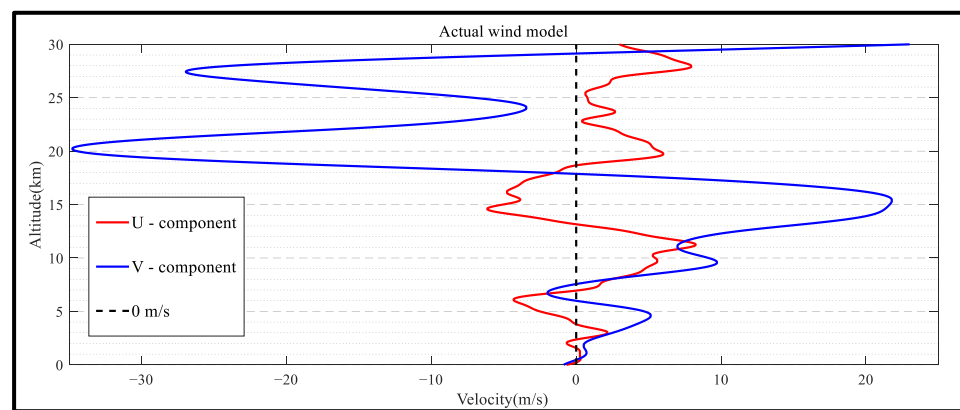
Table 3. Target parameters.

Parameter	Value
Target altitude (m)	17,450.0
The mass of the buoyant gas (kg)	6.81
The mass of the air (kg)	23.84
The mix ratio	3.50

The film material is polyethylene, which is commonly used in balloon engineering, and the optical properties are as follows:

3.4. Wind Model

This paper utilizes wind data detected by a meteorological balloon. As shown in Figure 6, the wind field model comprises the U-direction component and the V-direction component of the meteorological balloon, which serve as an input to the trajectory prediction model.

**Figure 6.** Actual wind model.

3.5. Analysis of Simulation

3.5.1. Dynamic Simulation

According to the parameters of the balloon and wind model, this paper simulates ascent. The results are shown below.

(1) Altitude simulation results

Figure 7 shows that the balloon gradually ascends to the target altitude through buoyancy. Eventually, the balloon fluctuates around the target height because of the adiabatic motion. The simulation results demonstrate that the balloon transitions from the

climb phase to the float phase. Simulation results show with various gas mixtures that an air–buoyant gas mixture for designated ceiling height technology is achievable.

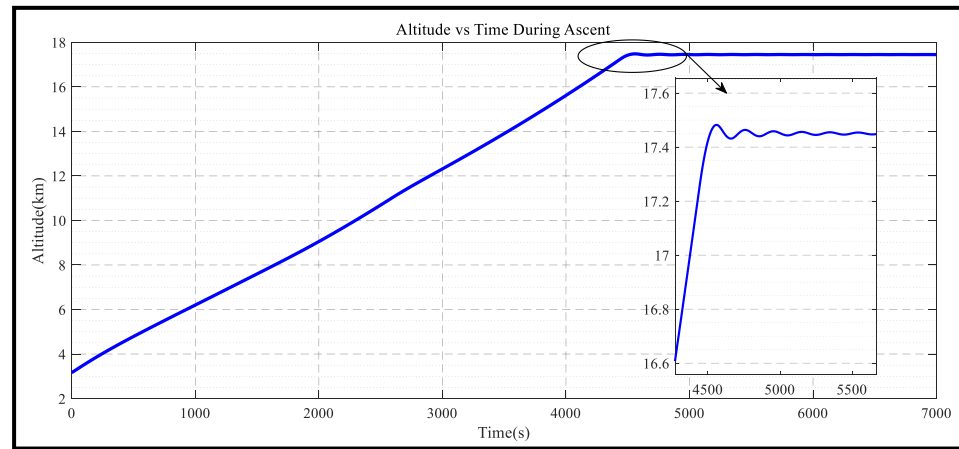


Figure 7. Altitude vs. time during ascent.

(2) Vertical velocity simulation results

Figure 8 demonstrates the vertical velocity change of the mixed-gas balloon during ascent. Within 30 s of launching, the vertical velocity increases sharply to 3.6 m/s because of the buoyancy. At 20 s, the vertical velocity begins to decrease because the inside temperature is lower than that of the outside atmosphere due to the fast expansion of the balloon volume. At 1400 s, the vertical velocity starts to increase. The main reason is that the balloon gas absorbs heat from the film through convection heat. At 2590 s, the velocity begins to decrease because the atmospheric temperature is almost constant when the balloon reaches 11 km, but the inside temperature decreases. From 2950 s, the vertical velocity increases until 4437 s, when the volume of the balloon reaches the maximum. Then the vertical velocity starts to decrease and eventually fluctuates around 0 m/s. The change in vertical velocity is consistent with the analytical results of Yang [49] and Du [35,50].

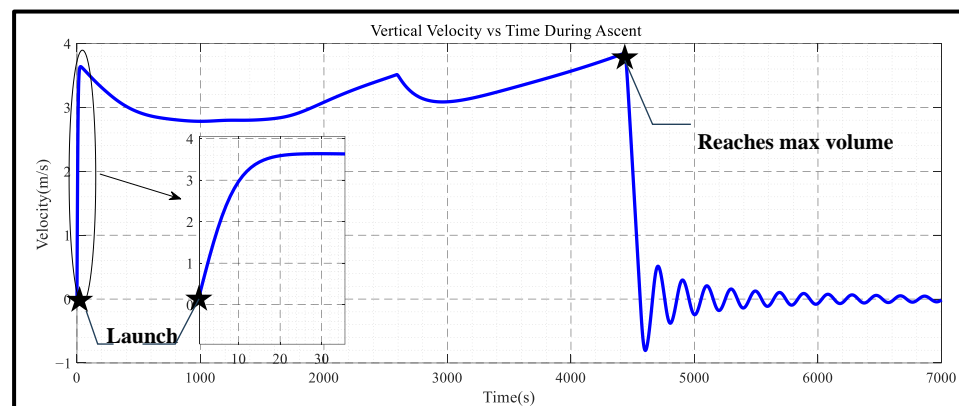


Figure 8. Vertical velocity vs. time during ascent.

(3) Trajectory prediction

This study investigates a trajectory prediction model that could serve balloon recovery. This paper utilizes wind field data detected by a meteorological balloon, which serves as an input to the trajectory prediction system. Combined with the 2.3 dynamic model, the system can accurately calculate wind force and predict the trajectory of a mixed-gas balloon as shown in Figures 9 and 10.

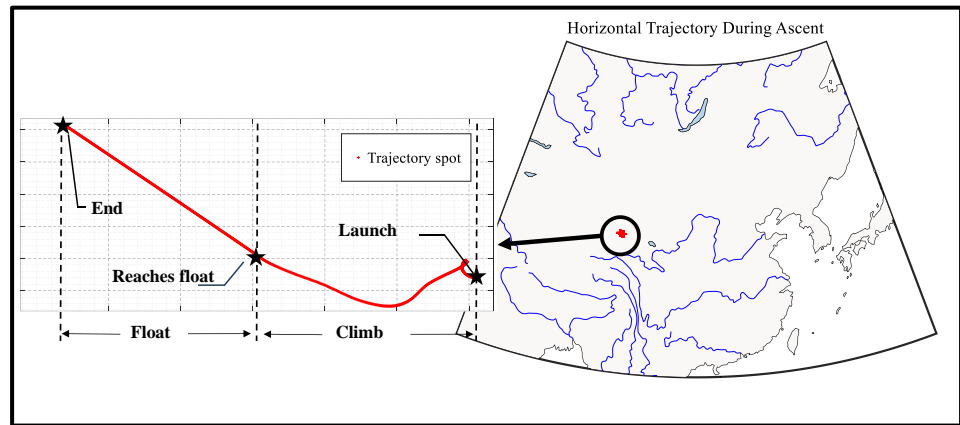


Figure 9. Horizontal trajectory during ascent.

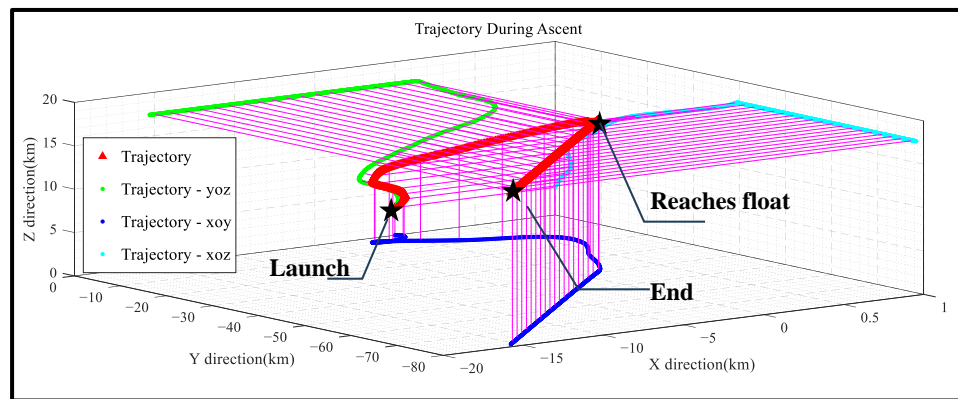


Figure 10. Trajectory during ascent.

3.5.2. Thermal Simulation

(1) Temperature

Figure 11 shows the temperature changes of the mixed-gas balloon during ascent. As the altitude increases, the temperatures of the balloon gas, film, and the environment decrease. Meanwhile, the temperature of the balloon gas is lower than the environmental temperature because of the balloon volume expansion, which is called the “supercooling phenomenon” [46].

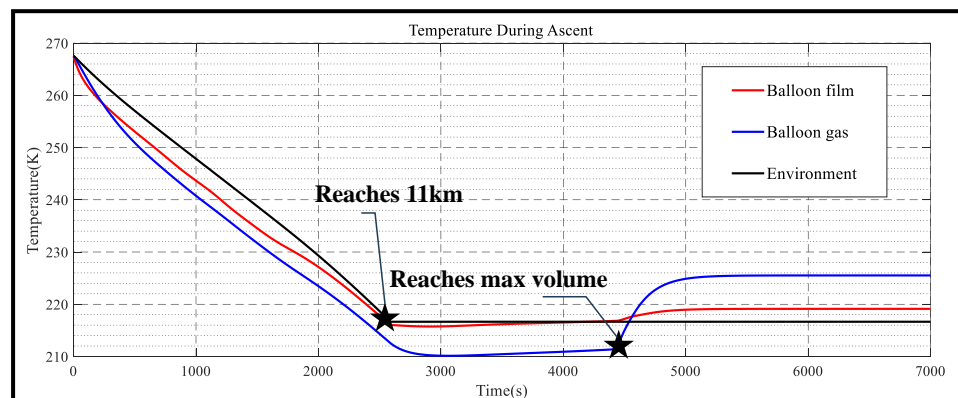


Figure 11. Temperature during ascent.

At 4437 s, the balloon volume expands to the maximum, and the temperature of the balloon gas gradually increases. Finally, the balloon gas temperature is greater than the

environment, which is called the “superheating phenomenon” [46]. The phenomena of supercooling and superheating are important for balloon design and material selection.

(2) Pressure

Figure 12 shows the ascent pressure difference value change of the mixed-gas balloon during ascent. Initially, as the balloon volume expands, the pressure inside the balloon equals that of the outside atmosphere. Consequently, within the period preceding 4437 s, the pressure difference value is 0 Pa. At 4437 s, the balloon volume expands to the maximum, and the gas is enclosed inside the balloon. Subsequently, the differential pressure value begins to increase and eventually fluctuates around 850 Pa.

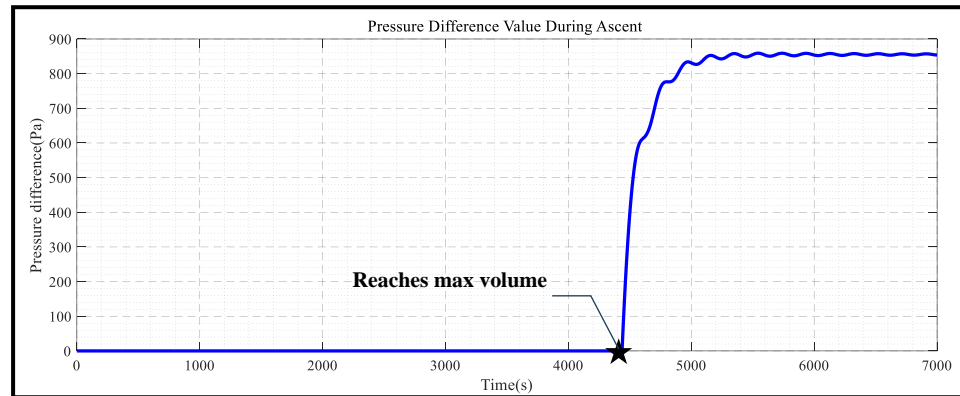


Figure 12. Pressure difference value during ascent.

It should be noted that this paper simulates the non-exhaust condition which is convenient for the selection of the film material. If the pressure difference value exceeds the safe range of the film, the test also considers decompression measures.

3.6. Target Height and Mixture Ratio Analysis

Figure 13 illustrates the gas mixture ratio corresponding to different volumes of balloons at different target altitudes. The simulation results show that for a certain volume of balloon, the mixture ratio increases as the target altitude increases. For a certain target altitude, the mixture ratio increases as the balloon volume increases.

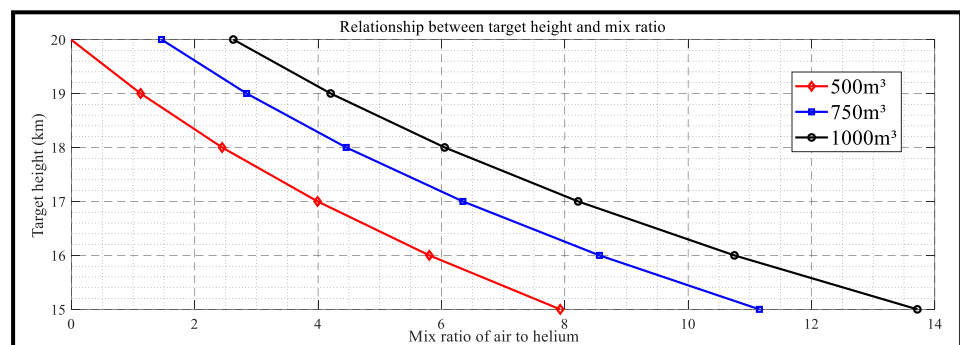


Figure 13. Analysis of target heights and mix ratio.

4. Flight Tests

4.1. System Composition

To further verify the feasibility of gas mixing for designated ceiling height technology and the accuracy of the simulation, the results of flight tests are presented here. The system is shown in Figure 14.

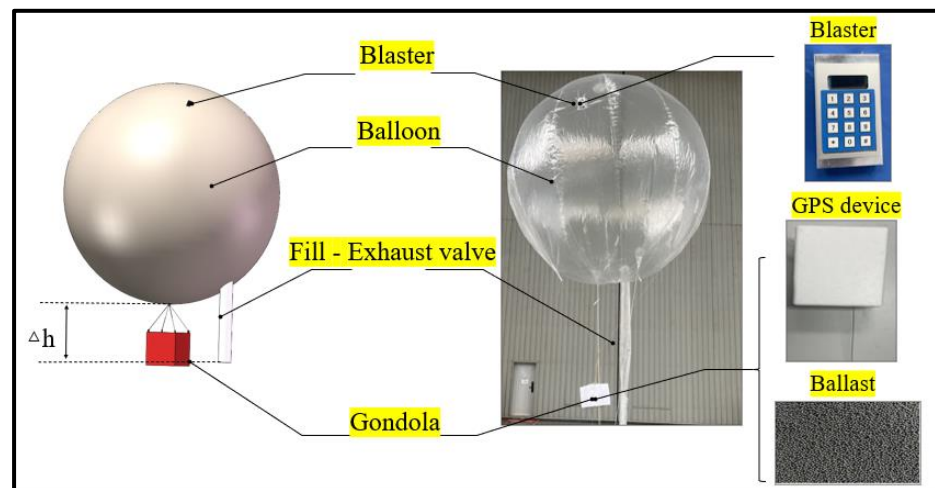


Figure 14. The system of flight test.

As shown in Figure 14, the flight test system mainly consists of three parts: balloon, gondola, and blaster. In the event of a large pressure difference value, commonly-used balloon materials would not be able to withstand it. To prevent the balloon from bursting, the test utilized the exhaust method commonly used in engineering. Additionally, to simplify the system, the exhaust pipe and the inflation pipe were designed as one line. Δh is the distance from the pipe bottom to the balloon bottom. Using this, according to the Bernoulli equation, the super-pressure value can be calculated. In addition, the gondola incorporated a GPS device with the sensor data sent down via telemetry, which was mainly used to collect the altitude, velocity, and position coordinates of the balloon.

4.2. Balloon Parameters

The maximum working altitude of the blaster is 8 km (8 km is the maximum altitude tested by the manufacturer). Taking into account the adiabatic motion and the vertical airflow that would cause the balloon to rise and fall, a target altitude below 7.5 km was chosen. In addition, the launch site altitude was 3180 m, and it was important to ensure that the balloon collected enough flight data for subsequent analysis. Therefore, a final target altitude of 7.2 km was chosen. The design parameters of the balloon were shown in Table 4.

Table 4. Balloon parameters and target parameters.

Parameter	Value
Target altitude (m)	7200
Mixture	Air and Helium
The mass of the buoyant gas (kg)	0.31
The mass of the air (kg)	1.51
The mix ratio	4.87
The mass of the gondola (kg)	0.60
The mass of the film (kg)	0.88
The mass of the system (kg)	3.30
Design volume (m ³)	5.00
The cross-sectional area of the exhaust (m ²)	0.0078
Super Pressure value (Pa)	20

The optical properties of the material are shown in Table 5.

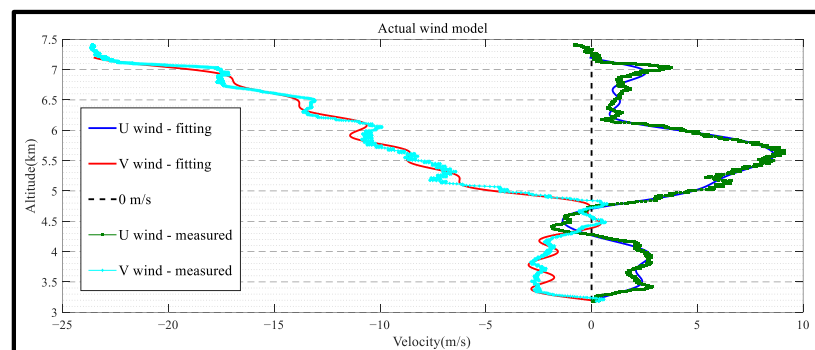
Table 5. Optical properties of PET composite film materials.

α	τ	α_{IR}	τ_{IR}
0.025	0.89	0.53	0.42

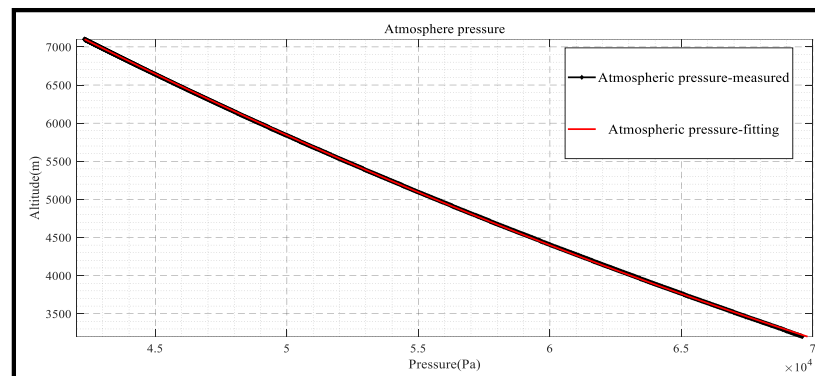
The optical properties of the material were obtained from the manufacturer.

4.3. Wind Field Environment

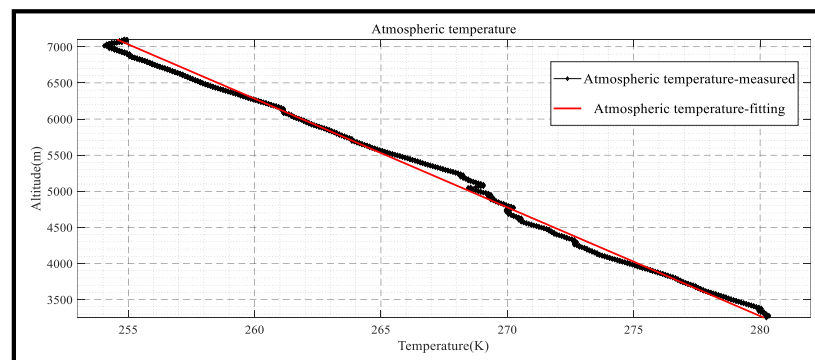
Before the test (LT: 4 October 2022, at 0:00), a meteorological balloon was launched to collect atmospheric data as shown in Figure 15. The data served as the input to the flight trajectory prediction system, which ensured that the test was safe and controllable.



(a)



(b)



(c)

Figure 15. Atmospheric data: (a) The actual wind model; (b) Atmospheric pressure; (c) Atmospheric temperature.

4.4. Flight Test

In order to increase the credibility of the test results, a second flight test was conducted (LT: 4 October 2022, 0:00 to 3:00). The results are shown below.

(1) Altitude

Figure 16 illustrates the results of the two test flight compared to the simulation. After launch, the height gradually increased under the effect of buoyancy. At 2000 s, the balloons entered the float phase. The test variations are consistent with the simulation. Meanwhile, the difference values are less than 350 m. The main reasons are the adiabatic motions and the fact that there would be vertical airflow at the target altitude. According to the results, there is a noticeable shift when the balloon starts to float after climbing to the target altitude. Therefore, it has been demonstrated that an air–buoyant gas mixture for designated ceiling height technology is feasible.

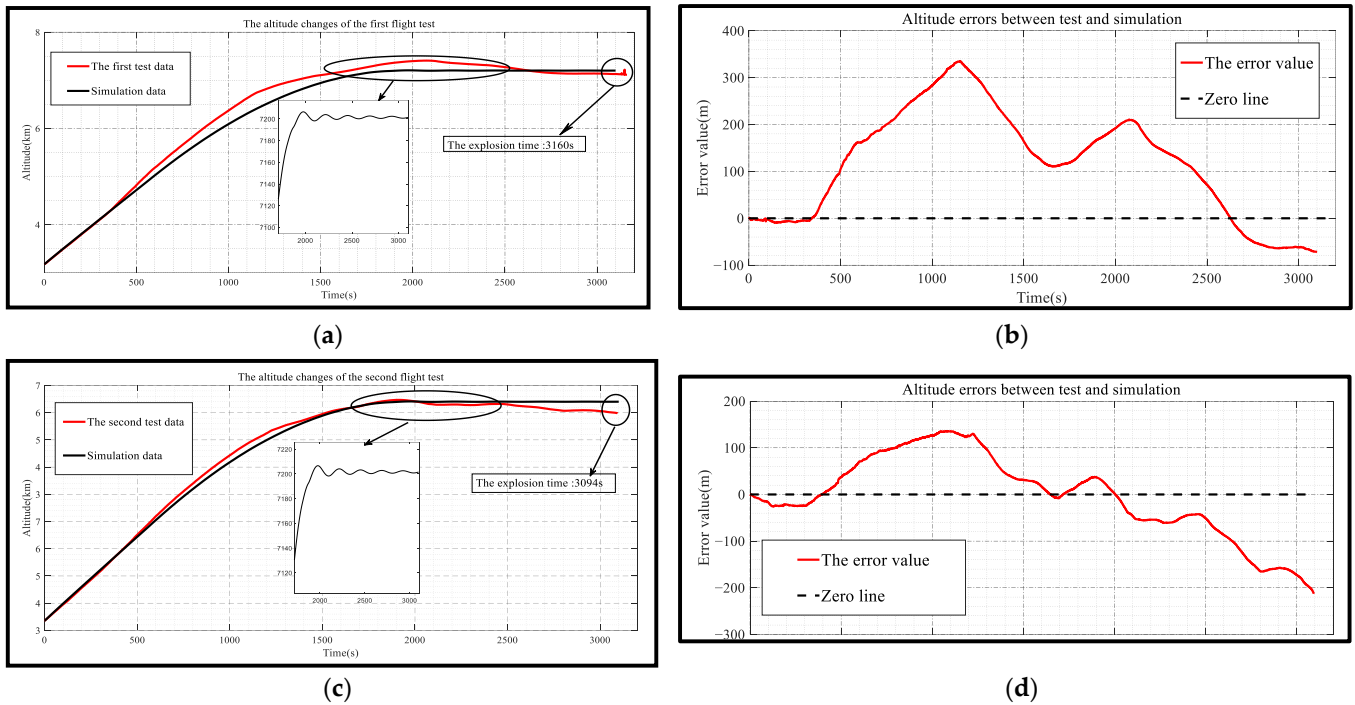


Figure 16. The altitude comparison: (a) The altitude changes of the first flight test; (b) The altitude errors between the first flight test and simulation; (c) The altitude changes of the second flight test; (d) The altitude errors between the second flight test and simulation.

(2) Vertical velocity

Figure 17 shows the vertical velocity comparison data with the simulation of two flight tests. The vertical velocity increases sharply to 3.2 m/s after launching. At 10 s, the vertical velocity begins to decrease because of the supercooling phenomenon. At 250 s, the vertical velocity starts to increase. The main reason is that the inside temperature begins to rise due to convective heat. At 565 s, the balloon volume expands to the maximum, which results in the vertical velocity beginning to decrease and eventually fluctuating around 0 m/s.

(3) Trajectory

The predicted trajectory of the balloon is obtained by converting the wind data to an equivalent wind force according to the 2.3 Dynamic model. The balloon trajectory data collected by the sensors are compared with the prediction as shown in Figure 18.

In Figure 18, the errors are less than 2.5 km ($\Delta d_1 = 2.44\text{km}$, $\Delta d_2 = 2.30\text{km}$) in horizontal distance. Further analysis of the reasons suggests that there is a discrepancy between the actual environment and the wind model used in the prediction model. On the other hand, there is an error in the blaster action. Therefore, the results verify the feasibility of the trajectory prediction model.

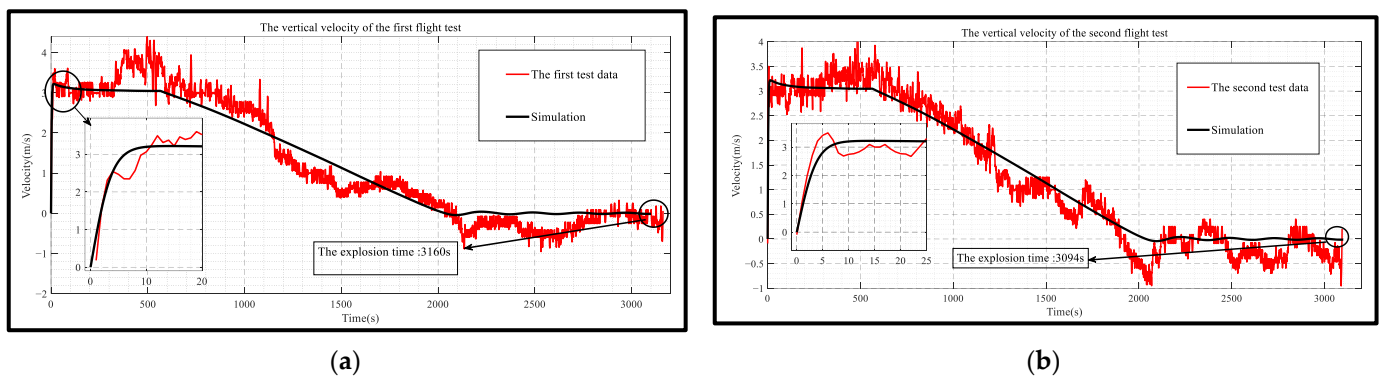


Figure 17. The vertical velocity: (a) The vertical velocity of the first flight test; (b) The vertical velocity of the second flight test.

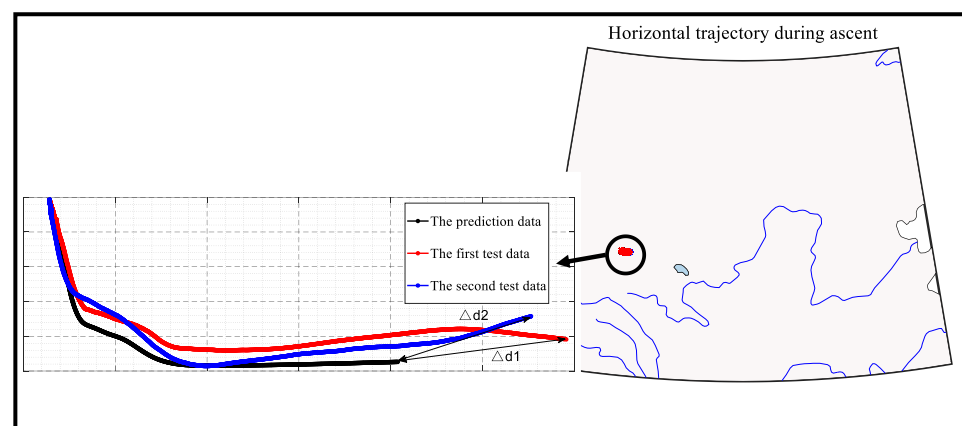


Figure 18. The horizontal trajectory comparison.

5. Conclusions

In this paper, we systematically investigated the ascending performance of mixed-gas balloons. Firstly, the theoretical model and simulation program were established. Subsequently, we conducted two flight tests, and the results verify the feasibility of an air–buoyant gas mixture for designated ceiling height technology. The main conclusions are shown as follows:

- (1) This paper provides a gas-mixing method for designated ceiling height technology of scientific balloons. The new method allows a single balloon system to be used for tests at multiple heights, which reduces the engineering cost. In addition, the mixing method can be extended to other types of aerostats.
- (2) The theoretical model of mixed-gas balloons is established, including the inflation model and the thermal-dynamic coupled model, which bridges the research gap of mixed-gas balloons.
- (3) We propose an accurate simulation method. Furthermore, the simulation was consistent with the flight tests in terms of speed, altitude, and trajectory. Additionally, the altitude error remained below 350 m, and the horizontal distance error at the endpoint was less than 2.5 km. These errors are allowed in balloon engineering to verify the accuracy of the simulation method.

This study investigates the ascending performance of mixed-gas balloons and provides valuable insights for further exploration in the field of mixed-gas aerostats.

Author Contributions: Conceptualization, S.C. and Y.Y.; methodology, S.C., H.Z. and R.Z. (Rong Zhao); software, S.C. and R.Z. (Rongchen Zhu); validation, S.C., D.Z. and R.Z. (Rong Zhao); formal analysis, S.C.; investigation, S.C., H.Z. and L.S.; resources, Y.Y., D.Z. and L.S.; data curation, S.C.; writing—

original draft preparation, S.C. and H.Z.; writing—review and editing, S.C., L.S. and H.Z.; visualization, S.C.; supervision, Y.Y.; project administration, Y.Y. and D.Z.; funding acquisition, Y.Y. and R.Z. (Rongchen Zhu). All authors have read and agreed to the published version of the manuscript.

Funding: This research was funded by National Key R&D Program of China, 2022YFB3903000, 2022YFB3903005. The article processing charge was funded by the Aerospace Information Research Institute, Chinese Academy of Sciences.

Data Availability Statement: Dataset available on request from the authors.

Acknowledgments: We would like to thank Yihan Li, Qiguang Yang, Zhanbo Li, Haotian Cheng, Ce Pang, and Zhijie Ke for their help with this experiment. Meanwhile, we would also like to thank our colleagues Yuxuan Du, Qiang Fu, Yi Jiang, Zhongzhen Jia, and Qianqian Du for providing the experimental equipment.

Conflicts of Interest: The authors declare no conflicts of interest.

Nomenclature

$Albedo$	Albedo factor	$Q_{IR-emit-gas}$	The heat emission of the buoyant gas (W)
A_{eff}	Effective surface area (m^2)	Q_{IR-int}	The thermal interchange of the film (W)
$A_{top-project}$	Top projection area (m^2)	$Q_{sun-gas}$	Solar radiation on the balloon gas (W)
A_{valve}	The cross-sectional area of the exhaust valve (m^2)	$Q_{sun-direct}$	The direct solar radiation (W)
c	Mass specific heat of the ingredients ($J/(kg \cdot K)$)	$Q_{sun-reflect}$	The reflected solar radiation (W)
c'	Volume specific heat of the ingredients ($J/(kg \cdot K)$)	r_{eff}	The effective balloon film reflectivity
c_v	Specific heat of the balloon gas ($J/(kg \cdot K)$)	r_n	Component of the volume
c_{film}	Specific heat of the film ($J/(kg \cdot K)$)	R	Specific heat constant
$C_{discharge}$	Exhaust parameter	R_{air}	Specific heat constant of air
C_D	Drag coefficient	R_{gas}	Specific heat constant of gas
C_m	Additional mass coefficient	S	Vertical projection area (m^2)
CF	Cloud factor	T	Environment temperature (K)
D	Drag force (N)	T_{air}	Air temperature (K)
$Diameter$	Balloon diameter (N)	T_{BB}	Equivalent temperature of blackbody radiation (K)
F_B	Buoyancy (N)	T_{film}	Film temperature (K)
g	Acceleration of gravity	T_{gas}	Balloon gas temperature (K)
g_n	Component of the mass	v	Velocity (m/s)
G	Binding coefficient	v_r	Relative velocity (m/s)
$HC_{external}$	Effective external convection coefficient	v_w	Wind velocity (m/s)
$HC_{internal}$	Effective internal convection coefficient	V_{air}	Air volume (m^3)
H_{force}	Heat transfer coefficient of external forced convection	$V_{balloon}$	Design volume of the balloon (m^3)
H_{free}	Heat transfer coefficient of external free convection	V_{gas}	Buoyant gas volume (m^3)
HRA	Hour angle	y	Molecular fraction
I_{sun}	Total solar intensity (W/m^2)	α	The balloon film absorption factor for the sun radiation
$I_{sun,z}$	Resultant solar intensity (W/m^2)	α_{IR}	Absorptivity of the IR radiation
k	Heat transfer coefficient	τ_{atm}	Atmospheric transmittance
m	Equivalent mass (kg)	τ_{IR}	Transmissivity of the IR radiation
m_{air}	Air mass (kg)	α_{ELV}	The sun elevation angle
$m_{balloon}$	Balloon mass (kg)	$\alpha_{eff-gas}$	Effective solar absorption factor of the balloon gas
$m_{balloon-gas}$	Balloon gas mass (kg)	δ	The declination angle
$m_{balloon-structure}$	Balloon structure mass (kg)	ΔP_{valve}	Exhaust trigger pressure difference (Pa)
m_{gas}	Buoyant gas mass (kg)	ε	Correction coefficient
$m_{payload}$	Payload mass (kg)	ε_{eff}	Effective emissivity factor
m_s	System mass (kg)	$\varepsilon_{eff-gas}$	Effective gas emissivity factor

m_v	Added mass (kg)	ϵ_{int}	Interchange effective emissivity factor
P	Environment pressure (Pa)	η	Mixed mass ratio of air and buoyant gas
q_{Albedo}	Diffuse planetary infrared flux (W/m^2)	ρ	Density (kg/m^3)
q_{sun}	Direct solar flux (W/m^2)	σ	Stefan–Boltzmann Number ($5.67 \times 10^{-8} W/(m^{-2} \cdot K^{-4})$)
$Q_{con-ext}$	External convection (W)	τ	The balloon film transmission factor for the sun radiation
$Q_{con-int}$	Internal convection (W)	τ_{IR}	Transmissivity of the IR radiation
$Q_{IR-earth\&sky}$	The effective IR radiation absorbance of the balloon film (W)	$\tau_{ViewFactor}$	Balloon surface area diffuse-radiant view factor
$Q_{IR-earth\&sky-gas}$	The effective IR radiation absorbance of the balloon gas (W)	ϕ	Interaction coefficient
$Q_{IR-emit}$	Balloon film emits heat radiation (W)	φ	The location altitude

References

- Zhang, Y.; Liu, D. Influences of Initial Launch Conditions on Flight Performance of High Altitude Balloon Ascending Process. *Adv. Space Res.* **2015**, *56*, 605–618. [\[CrossRef\]](#)
- Santos, J.S.; Garcia, D.; Cunha, M.L.; Góes, L.C.; Pant, R.S. Design and Flight Testing of an Autonomous Airship. In Proceedings of the 22nd AIAA Lighter-Than-Air Systems Technology Conference, Dallas, TX, USA, 22 June 2015; American Institute of Aeronautics and Astronautics: Reston, VA, USA, 2015.
- Smith, I.S. HiSentinel & Stratospheric Airship Design Sensitivity. KISS Workshop. 2013. Available online: <https://kiss.caltech.edu/workshops/airships/presentations/smith.pdf> (accessed on 19 April 2024).
- Rostami, M.; Kamoopuri, J.; Pradhan, P.; Chung, J. Development and Evaluation of an Enhanced Virtual Reality Flight Simulation Tool for Airships. *Aerospace* **2023**, *10*, 457. [\[CrossRef\]](#)
- Ma, Y.; Huang, J.; Yi, M. A Novel Technique for Predicting the Thermal Behavior of Stratospheric Balloon. *Int. J. Aerosp. Eng.* **2018**, *2018*, 7806036. [\[CrossRef\]](#)
- Angell, J.K.; Hoecker, W.H.; Dickson, C.R. Comparison of the Vertical Motions of Paired Tetroon Flights. *J. Appl. Meteorol. Climatol.* **1977**, *16*, 774–779. [\[CrossRef\]](#)
- Gilchrist, A. 1st Garp Global Experiment. *Meteorol. Mag.* **1979**, *108*, 129–134.
- Durre, I.; Vose, R.S.; Wuertz, D.B. Overview of the Integrated Global Radiosonde Archive. *J. Clim.* **2006**, *19*, 53–68. [\[CrossRef\]](#)
- Durre, I.; Yin, X.; Vose, R.S.; Applequist, S.; Arnfield, J. Enhancing the Data Coverage in the Integrated Global Radiosonde Archive. *J. Atmos. Ocean. Technol.* **2018**, *35*, 1753–1770. [\[CrossRef\]](#)
- Anand, D.; Kumar, B.S.; Ojha, D. TIFR Zero-Pressure Balloon Programme Crosses a Milestone. *Curr. Sci.* **2021**, *120*, 1672. [\[CrossRef\]](#)
- Corcos, M.; Hertzog, A.; Plougonven, R.; Podglajen, A. Observation of Gravity Waves at the Tropical Tropopause Using Superpressure Balloons. *JGR Atmos.* **2021**, *126*, e2021JD035165. [\[CrossRef\]](#)
- Jones, W.V. Scientific Ballooning: Past, Present and Future. *AIP Conf. Proc.* **2013**, *1516*, 229–233.
- Gonzalo, J.; López, D.; Domínguez, D.; García, A.; Escapa, A. On the Capabilities and Limitations of High Altitude Pseudo-Satellites. *Prog. Aerosp. Sci.* **2018**, *98*, 37–56. [\[CrossRef\]](#)
- Dai, Q.; Fang, X.; Li, X.; Tian, L. Performance Simulation of High Altitude Scientific Balloons. *Adv. Space Res.* **2012**, *49*, 1045–1052. [\[CrossRef\]](#)
- Zhang, H.; Yang, Y.; Cai, R. Dynamics Simulation of Folding Wing UAVs Launched from a High-Altitude Balloon Platform. *Proc. Inst. Mech. Eng. Part G J. Aerosp. Eng.* **2023**, *237*, 3072–3091. [\[CrossRef\]](#)
- Wang, X.; Zeng, G.; Yan, X.; Chen, W.; Li, K.; Yang, Y. A Feasibility Verification Scheme with Flight Analysis for Balloon-Borne Launched Unmanned Aerial Vehicles. In Proceedings of the 2020 3rd International Conference on Unmanned Systems (ICUS), Harbin, China, 27 November 2020; IEEE: Piscataway, NJ, USA, 2020; pp. 966–971.
- Schuler, T.K.; Bowman, D.C.; Izraelvitz, J.S.; Sofge, D.; Thangavelautham, J. Long Duration Flights in Venus' Atmosphere Using Passive Solar Hot Air Balloons. *Acta Astronaut.* **2022**, *191*, 160–168. [\[CrossRef\]](#)
- Cutts, J.; Aslam, S.; Atreya, S.; Baines, K.; Beauchamp, P.; Bellan, J.; Bowman, D.C.; Bugga, K.; Bullock, M.; Byrne, P.K.; et al. Scientific Exploration of Venus with Aerial Platforms. *Bull. AAS* **2021**, *53*, 1–8. [\[CrossRef\]](#)
- Rossi, F.; Saboia, M.; Krishnamoorthy, S.; Hook, J.V. Proximal Exploration of Venus Volcanism with Teams of Autonomous Buoyancy-Controlled Balloons. *Acta Astronaut.* **2023**, *208*, 389–406. [\[CrossRef\]](#)
- Garg, K.; Kuhn, T. Balloon Design for Mars, Venus, and Titan Atmospheres. *Appl. Sci.* **2020**, *10*, 3204. [\[CrossRef\]](#)
- Wei, J.; Ma, R.; Hou, X.; Zhen, D.; Tan, H. Analysis of the Thermodynamical Property of Super-Pressure Balloons. *Acta Mech.* **2019**, *230*, 1355–1366. [\[CrossRef\]](#)
- Saito, Y.; Akita, D.; Fuke, H.; Izutsu, N. Properties of Tandem Balloons Connected by Extendable Suspension Wires. *Adv. Space Res.* **2010**, *45*, 482–489. [\[CrossRef\]](#)
- Saleh, S.; He, W. New Design Simulation for a High-Altitude Dual-Balloon System to Extend Lifetime and Improve Floating Performance. *Chin. J. Aeronaut.* **2018**, *31*, 1109–1118. [\[CrossRef\]](#)

24. Cathey, H.M.; Tuttle, J.W.; Fairbrother, D.A.; Said, M.A. Qualification of the NASA Super Pressure Balloon. In Proceedings of the AIAA Balloon Systems Conference, Dallas, TX, USA, 22 June 2015; American Institute of Aeronautics and Astronautics: Reston, VA, USA, 2015.
25. Cathey, H.M. The NAS+A Super Pressure Balloon—A Path to Flight. *Adv. Space Res.* **2009**, *44*, 23–38. [[CrossRef](#)]
26. Dubourg, V.; Louvel, S.; Venel, S.; Vacher, F.; Thoumieux, F.; Deschamps, A. An Update of the CNES Stratospheric Balloon Activities. In Proceedings of the Aerospace Europe Conference 2023—10th EUCASS—9th CEAS, Lausanne, Switzerland, 9 July 2023. [[CrossRef](#)]
27. McKinney, T.; Perlaky, N.; Crawford, A.; Brown, B.; Newchurch, M.J. Methodology, Deployment, and Performance of Pico Balloons in Antarctica. *J. Atmos. Ocean. Technol.* **2023**, *40*, 1277–1290. [[CrossRef](#)]
28. McKinney, T.; Perlaky, N.; Danielson, E.; Mohammed, A.; Lee, J.; O’Bryan, B.; Stoll, C.; Hochmuth, C.; Gallien, T.; Kerr, S.; et al. Around the World They Go: Circumnavigating Balloon Satellites! *Bull. Am. Meteorol. Soc.* **2023**, *104*, E192–E207. [[CrossRef](#)]
29. McKinney, T.; Perlaky, N.; Newchurch, M.; Brown, B. Insights on Polar Day Antarctica Radio Propagation Using Amateur Radio Beacons on Circumnavigating Balloons. *Atmosphere* **2023**, *14*, 1118. [[CrossRef](#)]
30. Wilke, C. Diffusional properties of multicomponent gases. *Chem. Eng. Prog.* **1950**, *46*, 95–104.
31. Tong, J. Viscosity and thermal conductivity of gas mixtures and liquid mixtures. *Chem. Eng.* **1977**, *6*, 66–84.
32. Woo, K.W.; Yeo, S.I. Dalton’s Law vs., Amagat’s Law for the Mixture of Real Gases. *SNU J. Educ. Res.* **1995**, *5*, 127–134.
33. Farley, R. Balloon Ascent: 3-D Simulation Tool for the Ascent and Float of High-Altitude Balloons. In Proceedings of the AIAA 5th ATIO and 16th Lighter-Than-Air Sys Tech. and Balloon Systems Conferences, Arlington, VA, USA, 26 September 2005; American Institute of Aeronautics and Astronautics: Reston, VA, USA, 2015.
34. Saleh, S.; He, W. Ascending Performance Analysis for High Altitude Zero Pressure Balloon. *Adv. Space Res.* **2017**, *59*, 2158–2172. [[CrossRef](#)]
35. Du, H.; Li, J.; Zhu, W.; Qu, Z.; Zhang, L.; Lv, M. Flight Performance Simulation and Station-Keeping Endurance Analysis for Stratospheric Super-Pressure Balloon in Real Wind Field. *Aerosp. Sci. Technol.* **2019**, *86*, 1–10. [[CrossRef](#)]
36. Jiang, Y.; Lv, M.; Li, J. Station-Keeping Control Design of Double Balloon System Based on Horizontal Region Constraints. *Aerosp. Sci. Technol.* **2020**, *100*, 105792. [[CrossRef](#)]
37. Du, H.; Lv, M.; Zhang, L.; Zhu, W.; Wu, Y.; Li, J. Energy Management Strategy Design and Station-Keeping Strategy Optimization for High Altitude Balloon with Altitude Control System. *Aerosp. Sci. Technol.* **2019**, *93*, 105342. [[CrossRef](#)]
38. Liu, Y.; Xu, Z.; Du, H.; Lv, M. Increased Utilization of Real Wind Fields to Improve Station-Keeping Performance of Stratospheric Balloon. *Aerosp. Sci. Technol.* **2022**, *122*, 107399. [[CrossRef](#)]
39. Liao, J.; Yang, Z.; Li, J.; Luo, S. Shape and Envelope Tension Prediction of Natural Shaped High Altitude Balloons. *Aerosp. Sci. Technol.* **2021**, *117*, 106963. [[CrossRef](#)]
40. Jiang, Y.; Lv, M.; Chen, X.; Wu, Y. An Optimization Approach for Improving the Solar Array Output Power of Stratospheric Aerostat. *Aerosp. Sci. Technol.* **2021**, *118*, 106916. [[CrossRef](#)]
41. Zhang, J.; Yang, X.; Deng, X.; Lin, H. Trajectory Control Method of Stratospheric Airships Based on Model Predictive Control in Wind Field. *Proc. Inst. Mech. Eng. Part G J. Aerosp. Eng.* **2019**, *233*, 418–425. [[CrossRef](#)]
42. Carlson, L.A.; Horn, W.J. New Thermal and Trajectory Model for High-Altitude Balloons. *J. Aircr.* **1983**, *20*, 500–507. [[CrossRef](#)]
43. Zhang, L.; Li, J.; Jiang, Y.; Du, H.; Zhu, W.; Lv, M. Stratospheric Airship Endurance Strategy Analysis Based on Energy Optimization. *Aerosp. Sci. Technol.* **2020**, *100*, 105794. [[CrossRef](#)]
44. Li, X.; Fang, X.; Dai, Q. Research on Thermal Characteristics of Photovoltaic Array of Stratospheric Airship. *J. Aircr.* **2011**, *48*, 1380–1386. [[CrossRef](#)]
45. Li, J.; Lv, M.; Sun, K.; Zhu, W. Thermal Insulation Performance of Lightweight Substrate for Solar Array on Stratospheric Airships. *Appl. Therm. Eng.* **2016**, *107*, 1158–1165. [[CrossRef](#)]
46. Du, H.; Lv, M.; Li, J.; Zhu, W.; Zhang, L.; Wu, Y. Station-Keeping Performance Analysis for High Altitude Balloon with Altitude Control System. *Aerosp. Sci. Technol.* **2019**, *92*, 644–652. [[CrossRef](#)]
47. Jiang, Y.; Lv, M.; Zhu, W.; Du, H.; Zhang, L.; Li, J. A Method of 3-D Region Controlling for Scientific Balloon Long-Endurance Flight in the Real Wind. *Aerosp. Sci. Technol.* **2020**, *97*, 105618. [[CrossRef](#)]
48. Abe, T.; Imamura, T.; Izutsu, N.; Yajima, N. *Scientific Ballooning*; Springer: New York, NY, USA, 2009; ISBN 978-0-387-09725-1.
49. Yang, X.; Zhang, W.; Hou, Z. Improved Thermal and Vertical Trajectory Model for Performance Prediction of Stratospheric Balloons. *J. Aerosp. Eng.* **2015**, *28*, 04014075. [[CrossRef](#)]
50. Huafei, D.; YiFei, W.; Mingyun, L. Ascent Performance Analysis for High Altitude Super Pressure Balloon in Real Wind Field. In Proceedings of the 2019 IEEE 10th International Conference on Mechanical and Aerospace Engineering (ICMAE), Brussels, Belgium, 22–25 July 2019; IEEE: Piscataway, NJ, USA, 2019; pp. 102–107.

Disclaimer/Publisher’s Note: The statements, opinions and data contained in all publications are solely those of the individual author(s) and contributor(s) and not of MDPI and/or the editor(s). MDPI and/or the editor(s) disclaim responsibility for any injury to people or property resulting from any ideas, methods, instructions or products referred to in the content.